PHILOSOPHICAL TRANSACTIONS A

rsta.royalsocietypublishing.org

Review

Article submitted to journal

Subject Areas:
computational mechanics, computational physics, computational modelling and simulation

Keywords:
computational methods, phase transition, phase field modelling

Author for correspondence:
Hector Gomez
e-mail: hectorgomez@purdue.edu

THE ROYAL SOCIETY PUBLISHING

A review on computational modelling of phase-transition problems

Hector Gomez, Miguel Bures and Adrian Moure

School of Mechanical Engineering, Purdue University, 585 Purdue Mall, West Lafayette, 47907 IN, USA

Phase-transition problems are ubiquitous in science and engineering. They have been widely studied via theory, experiments and computations. This paper reviews the main challenges associated to computational modelling of phase-transition problems, addressing both model development and numerical discretization of the resulting equations. We focus on classical phase-transition problems, including liquid-solid, gas-liquid and solid-solid transformations. Our review has a strong emphasis on the treatment of interfacial phenomena and the phase-field method.

1. Introduction

Perhaps the most classical example of a phase transition is a change between the gaseous, liquid and solid phases of a single component, for example, ice melting to liquid water, steam condensing into liquid water or dry ice subliming to gaseous CO_2. The term phase transition is also used more broadly to describe phenomena that are at a first glance very different from the classical example of, e.g., liquid-to-gas transformations, but share many important properties. For example, we usually consider a phase transition the process whereby a magnet loses its magnetic properties upon a temperature increase. For most phase transformations problems, the appearance of interfaces is inherent to the problem. From a modelling point of view, the presence of interfaces transforms the problem into a free-boundary problem. Free-boundary problems are very difficult to treat mathematically and computationally. Here, we review different approaches to computational modelling of phase-transition problems. By computational modelling, we refer to both model development and numerical discretization of the resulting equations. Due to space limitations, we focus on specific examples of liquid-solid,

liquid-gas and solid-solid transformations. This allows us to cover classical examples such as solidification of a pure material, vaporization and condensation, martensitic transformations and grain growth. Our review has a strong emphasis on the phase-field method.

2. The phase-field approach

(a) Mean curvature flow

Let us consider a surface $\Gamma(t)$ that evolves in time. We say that the surface evolves by mean curvature flow if the normal velocity of a point on the surface is proportional to the mean curvature of the surface at that point. Computing the time evolution of Γ requires a parameterization of the surface which changes in time. This may initially look like a very simple problem to treat, but even in this case, the situation is quite challenging because it is known that mean curvature flow develops singularities and these are usually unavoidable [1]. For example, for an initial closed surface, the flow contracts the surface until it collapses to a point. Another potential complication is that the topology of the surface can change through the evolution. These two examples illustrate the challenge of treating mean curvature flow computationally by using an explicit parametric representation of the surface. Mean curvature flow may be understood as a very simple phase transition problem. More physically relevant phase transition problems have a higher level of complexity and may involve the solution of partial differential equations (PDEs) in the interior and exterior of the surface. Because the surface evolves in time, the numerical approximation of the PDEs requires geometrically flexible computational methods (e.g., the finite element method) and a procedure to update the mesh. Interface motion is usually not only controlled by the geometry of the surface (like in mean curvature flow), but also by the value of the unknowns to be solved in the interior and exterior of the surface. For these reasons, an alternative formulation that does not require an explicit parameterization of the surface is desirable. There are multiple approaches that permit to avoid the surface parameterization [2]. In our opinion, the two most successful are the level set approach [3–5] and the phase-field method [6–9]. Both formulations employ an auxiliary field $\phi(\boldsymbol{x},t)$, which is a function of space and time. The surface $\Gamma(t)$ is defined as $\Gamma(t) \equiv \{\boldsymbol{x} \mid \phi(\boldsymbol{x},t) = 0\}$. Level set methods usually define ϕ as $\phi(\boldsymbol{x},t) = d(\boldsymbol{x},\Gamma(t))$, where $d(\boldsymbol{x},\Gamma(t))$ represents the signed distance from $\boldsymbol{x}$ to Γ at time t. The phase-field method, however, defines ϕ as a hyperbolic tangent function of d, such that $\phi(\boldsymbol{x},t) = \tanh\left(\frac{d(\boldsymbol{x},\Gamma(t))}{\sqrt{2}\epsilon}\right)$, where ϵ is a length scale. The phase field may be understood as a *diffuse interface* between the phases that replaces the original *sharp interface*. The length scale ϵ is a measure of the thickness of the diffuse interface. As $\epsilon \to 0$, we recover the sharp-interface limit. We favor the phase-field approach because, in addition to the purely geometric interpretation that we have just described, it may also be understood as a generalized approach to thermomechanics that permits to derive mathematical models for interface problems by using the Coleman-Noll approach and classical balance laws for mass, linear momentum, angular momentum and energy [6]. This has led to an enormous number of applications of the phase-field method to material science [10,11], solid mechanics [12–15], fluid mechanics [7,16–19], biomechanics [20–24] and interface problems in general [25–28].

Next, we show how to derive a phase-field formulation of mean curvature flow [29,30]. The mathematical formulation of mean curvature flow can be stated as follows: Let us assume that the time evolving surface $\Gamma(t) \subset \mathbb{R}^3$ is defined parametrically as $\Gamma(t) \equiv \{\boldsymbol{x}_\Gamma(\boldsymbol{p},t) \mid \boldsymbol{p} \in \mathcal{R}_p\}$ where $\boldsymbol{p}$ represents two parametric coordinates defined in suitable ranges $\mathcal{R}_p$. Mean curvature flow can be defined as

$$\frac{\partial \boldsymbol{x}_\Gamma}{\partial t}(\boldsymbol{p},t) = -\gamma\boldsymbol{\kappa}, \tag{2.1}$$

where $\boldsymbol{\kappa}$ is the curvature vector of the surface and γ is a positive constant. To derive a phase-field formulation of mean curvature flow, we introduce the phase-field

$$\phi(\boldsymbol{x},t) = f\left(\frac{d(\boldsymbol{x},\Gamma(t))}{\sqrt{2}\epsilon}\right), \quad \text{where} \quad f(z) = \tanh(z). \tag{2.2}$$

We adopt the sign convention that d is positive outside $\Gamma(t)$ and negative inside. The unit outward normal vector to $\Gamma(t)$ can be defined as $\boldsymbol{n} = \nabla d$ and the mean curvature as $\kappa_m = \frac{\Delta d}{2}$. The spatial derivatives of the phase field can be computed as

$$\frac{\partial \phi}{\partial x_i} = f'\left(\frac{d}{\sqrt{2}\epsilon}\right)\frac{\partial d}{\partial x_i}\frac{1}{\sqrt{2}\epsilon}, \quad \frac{\partial^2 \phi}{\partial x_i \partial x_j} = \frac{1}{2\epsilon^2} f''\frac{\partial d}{\partial x_i}\frac{\partial d}{\partial x_j} + \frac{1}{\sqrt{2}\epsilon} f'\frac{\partial^2 d}{\partial x_i \partial x_j}. \tag{2.3}$$

Next, by using the identities $f = \phi$, $f' = 1 - f^2$ and $f'' = -2ff'$, we obtain, from Eq. (2.3),

$$\nabla d = \boldsymbol{n} = \frac{\sqrt{2}\epsilon}{1-\phi^2}\nabla\phi, \quad \text{and} \quad \frac{1}{2}\Delta d = \kappa_m = \frac{\epsilon}{\sqrt{2}(1-\phi^2)}\left(\Delta\phi + \frac{2\phi}{1-\phi^2}|\nabla\phi|^2\right). \tag{2.4}$$

Let us define the function $\tilde{\phi}(t) = \phi(\boldsymbol{x}_\Gamma(\cdot, t), t)$, which is identically zero according to the definition of the phase field; see Eq. (2.2). Using the chain rule we can write

$$0 = \frac{\mathrm{d}\tilde{\phi}}{\mathrm{d}t} = \nabla\phi\frac{\partial \boldsymbol{x}_\Gamma}{\partial t} + \frac{\partial \phi}{\partial t}. \tag{2.5}$$

The motion of an interface is determined by its normal velocity, which in this case, can be computed as

$$\frac{\partial \boldsymbol{x}_\Gamma}{\partial t}\cdot\boldsymbol{n} = \frac{\sqrt{2}\epsilon}{1-\phi^2}\frac{\partial \boldsymbol{x}_\Gamma}{\partial t}\cdot\nabla\phi = -\frac{\sqrt{2}\epsilon}{1-\phi^2}\frac{\partial \phi}{\partial t}, \tag{2.6}$$

where we used Eqs. (2.4) and (2.5). Then, substituting Eqs. (2.4) and (2.6) into (2.1), we obtain the phase-field formulation of mean curvature flow

$$\frac{\partial \phi}{\partial t} = \frac{\gamma}{2}\left(\Delta\phi + \frac{2\phi}{1-\phi^2}|\nabla\phi|^2\right). \tag{2.7}$$

To write Eq. (2.7) as the classical Allen-Cahn equation, we need to introduce the function $W(\phi) = \frac{1}{4}(1-\phi^2)^2$. From the relation $f' = 1 - f^2$, it may be shown that $\frac{\epsilon^2}{2}|\nabla\phi|^2 = \frac{1}{4}(1-\phi^2)^2$. This implies that $\frac{2\phi}{1-\phi^2}|\nabla\phi|^2 = -\frac{W'(\phi)}{\epsilon^2}$ and the phase-field formulation of mean curvature flow becomes

$$\frac{\partial \phi}{\partial t} = \frac{\gamma}{2}\left(\Delta\phi - \frac{W'(\phi)}{\epsilon^2}\right), \tag{2.8}$$

which corresponds to the classical Allen-Cahn equation [31,32].

(b) Thermomechanics approach to Allen-Cahn

The Allen-Cahn equation can be derived as an approximation to mean curvature flow, but also from fundamental balance laws and the Coleman-Noll approach [33,34]. The Coleman-Noll method starts by postulating a free energy functional that is enforced to decrease as the solution evolves in time. This is a rational approach to impose restrictions to the constitutive relations. The energy functional may be expressed in terms of the free energy density Ψ as $\mathcal{F}[\phi] = \int_\Omega \Psi \mathrm{d}x$, where Ω denotes the spatial domain. The free-energy density Ψ is assumed to belong to the constitutive class $\Psi = \widehat{\Psi}(\phi, \nabla\phi)$. The energy-dissipation property that we postulate can be expressed as $\dot{\mathcal{F}} = \mathcal{W}(\Omega) - \mathcal{D}(\Omega)$, where $\dot{\mathcal{F}}$ denotes the time derivative of $\mathcal{F}$. In addition, $\mathcal{W}(\Omega)$ is referred to as the *working* term and accounts for external forces or energy supplies coming through the boundary of Ω. The *dissipation* term, $\mathcal{D}(\Omega)$ must be non-negative for all conceivable processes. The Allen-Cahn equation represents non-conservative phase dynamics. Therefore, the mass balance equation may be expressed as

$$\frac{\partial \phi}{\partial t} = -R, \tag{2.9}$$

where the function R is determined to ensure energy dissipation. The constitutive class of R is given by $R = \widehat{R}(\phi, \nabla\phi, \mu)$, where $\mu = \frac{\partial \widehat{\Psi}}{\partial \phi} - \nabla\cdot\left(\frac{\partial \widehat{\Psi}}{\partial \nabla\phi}\right)$ is the variational derivative of $\mathcal{F}$ with

respect to ϕ. By using the definition of the free energy $\mathcal{F}$ and the chain rule, we obtain

$$\dot{\mathcal{F}} = \frac{\mathrm{d}}{\mathrm{d}t}\int_\Omega \Psi \,\mathrm{d}x = \int_\Omega -\mu R \,\mathrm{d}x + \int_{\partial\Omega} \frac{\partial \widehat{\Psi}}{\partial \nabla\phi}\cdot \boldsymbol{n}\frac{\partial \phi}{\partial t}\,\mathrm{d}a, \tag{2.10}$$

where $\partial\Omega$ is the boundary of Ω and $\boldsymbol{n}$ denotes the unit outward normal to $\partial\Omega$. In Eq. (2.10), we identify $\mathcal{D}(\Omega) = \int_\Omega \mu R \,\mathrm{d}x$ and the remaining term on the right-hand side as $\mathcal{W}(\Omega)$. To achieve energy dissipation, we take $R = m(\phi)\mu$, with $m(\phi) \geq 0$. If we define Ψ using the classical Ginzburg-Landau energy, that is, $\Psi = W(\phi) + \frac{\epsilon}{2}|\nabla\phi|^2$, then substituting $R = m(\phi)\mu$ in Eq. (2.9), we get the canonical Allen-Cahn equation

$$\frac{\partial \phi}{\partial t} = -m(\phi)\left(W'(\phi) - \epsilon^2 \Delta\phi\right). \tag{2.11}$$

Taking $m(\phi) = \frac{\gamma}{2\epsilon^2}$, we recover the phase-field form of mean curvature flow; see Eq. (2.8).

3. Liquid-solid phase transformations

Liquid-solid phase transformations usually refer to solidification and melting. This type of phase transformations have been widely studied in the literature [28,35,36].

(a) Generalized Stefan problem

The generalized Stefan problem considers a solid-liquid system in the open, spatial domain Ω. The spatial domain $\overline{\Omega}$ can be decomposed as $\overline{\Omega} = \overline{\Omega_s \cup \Omega_\ell}$, where Ω_ℓ and Ω_s denote, respectively, the liquid and solid subdomains. Due to the phase transformations, both Ω_ℓ and Ω_s change with time and their time evolution is actually one of the unknowns of the problem. The solid-liquid interface $\Gamma_{\ell s}$ is defined as $\Gamma_{\ell s} = \overline{\Omega_\ell} \cap \overline{\Omega_s}$. The generalized Stefan problem can be expressed as

$$\rho\frac{\partial e}{\partial t} + \nabla\cdot\boldsymbol{q} = 0 \quad \text{in} \quad \Omega_s \cup \Omega_\ell, \tag{3.1}$$

$$\rho\ell V_n = [\![\boldsymbol{q}]\!]\cdot\boldsymbol{n}_{\ell s} \quad \text{on} \quad \Gamma_{\ell s}, \tag{3.2}$$

$$[\![\theta]\!] = 0 \quad \text{on} \quad \Gamma_{\ell s}, \tag{3.3}$$

$$\frac{\theta_m - \theta}{\theta_m}\rho H = \sigma(2\kappa_m + \omega V_n) \quad \text{on} \quad \Gamma_{\ell s}, \tag{3.4}$$

where ρ denotes density, $e = C_v\theta + \ell\chi_\ell$ is internal energy per unit mass, θ is the temperature, C_v is heat capacity per unit mass, ℓ is specific latent heat (energy per unit mass) and χ_ℓ is a characteristic function of the liquid phase, i.e., a discontinuous function that takes the values $+1$ in the liquid phase and 0 in the solid phase. We use Fourier equation, so that $\boldsymbol{q} = -k\nabla\theta$ where k is the thermal conductivity (energy per unit length, per unit time and per unit temperature). V_n is the normal velocity of the interface (positive if directed towards the liquid), $[\![\boldsymbol{q}]\!]$ is the heat flux jump across the interface with the sign convention that $[\![f]\!] = f_s - f_\ell$ for any function quantity that is discontinuous across the interface, $\boldsymbol{n}_{\ell s}$ is the unit normal to $\Gamma_{\ell s}$ pointing towards the liquid, θ_m is the melting temperature, H represents the interfacial enthalpy per unit mass, ω is the kinetic undercooling coefficient, κ_m is the mean curvature of the interface (positive for spherical solid crystals) and σ is the surface tension. By following the same procedure employed to derive a phase-field formulation of mean curvature flow we can obtain a phase-field approximation to the generalized Stefan problem that reads as

$$\rho C_v\frac{\partial\theta}{\partial t} + \ell\rho h'(\phi)\frac{\partial\phi}{\partial t} = \nabla\cdot\big(k(\phi)\nabla\theta\big); \quad \omega\frac{\partial\phi}{\partial t} = \Delta\phi - \frac{W'(\phi)}{\epsilon^2} + \frac{\rho H}{\sqrt{2}\epsilon\sigma}G(\phi)\frac{\theta-\theta_m}{\theta_m}. \tag{3.5}$$

Here, ϕ is a phase field that transitions smoothly from -1 in the solid to $+1$ in the liquid, h is a monotone interpolatory function that verifies $h(+1) = 1$, $h(-1) = 0$, e.g., $h(\phi) = \frac{1}{2}(1+\phi)$ and W is the double-well potential introduced in Sect. 2. The thermal conductivity is a function of the phase-field to account for a potentially different thermal conductivity of the liquid and solid phases. We take a function that satisfies $k(+1) = k_\ell$ and $k(-1) = k_s$, for example, $k(\phi) = \frac{1}{2}(1+\phi)k_\ell + \frac{1}{2}(1-\phi)k_s$. The function $G(\phi)$ vanishes in the pure phases. There are multiple

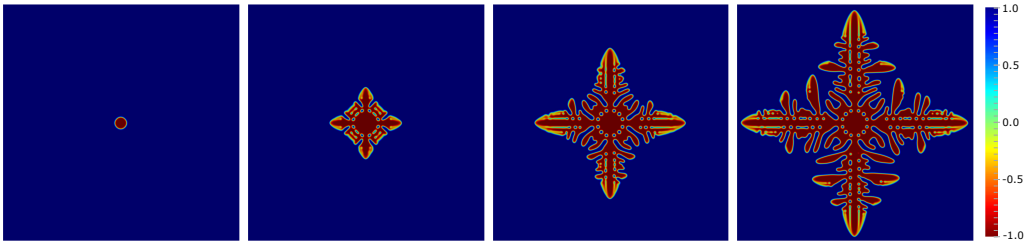

Figure 1: Crystal growth on the two-dimensional domain $\Omega = [0, L]^2$ with $L = 0.1\,\mathrm{cm}$. We used a uniform mesh with 512^2 $\mathcal{C}^1$-quadratic elements. We employed the parameters $\rho = 8.91\,\mathrm{g\,cm^{-3}}$, $C_v = 0.6083\,\mathrm{J\,K^{-1}\,g^{-1}}$, $\ell = 274.98\,\mathrm{J\,g^{-1}}$, $k_s = k_\ell = 0.8401\,\mathrm{J\,K^{-1}\,cm^{-1}\,s^{-1}}$, $\omega = 130\,\mathrm{s\,cm^{-2}}$, $\epsilon = 2 \cdot 10^{-4}\mathrm{cm}$, $H = -4.751\,\mathrm{J\,g^{-1}}$, $\overline{\sigma} = 3.7 \cdot 10^{-5}\mathrm{J\,cm^{-2}}$, $\theta_m = 1728\,\mathrm{K}$, $\delta = 0.05$, $\alpha_0 = \pi/4$ and $q = 4$.

possibilities for $G(\phi)$. Depending on the functional form that we choose for $G(\phi)$, the phase-field formulation will converge faster or slower to the generalized Stefan problem. Common choices in the literature are $G(\phi) = 1 - \phi^2$ and $G(\phi) = (1 - \phi^2)^2$. Here, we will use the second one. To attain good agreement between simulations and experiments, it is common to introduce anisotropy in the material surface tension by assuming that σ depends on the unit normal to the liquid-solid interface. We use the expression $\sigma/\overline{\sigma} = 1 + \delta\cos[q(\alpha - \alpha_0)]$, where $\overline{\sigma}$ is the mean value of σ, δ is the strength of the anisotropy, q is the mode number and α_0 is the preferred angle. The angle of the normal to the surface, α, can be easily defined from the phase field. Fig. 1 shows the results of a simulation performed using isogeometric analysis [37]. The computation shows how a crystal located in an undercooled region grows creating a dendritic pattern.

(b) Free-energy approach to solidification

(i) Wang's solidification model

Phase-field models of solidification can also be derived using thermomechanics [38,39]. The internal energy and entropy of any subvolume $\mathcal{V}$ of the system of interest can be defined as

$$\mathcal{E} = \int_{\mathcal{V}} \rho\, e\, \mathrm{d}x, \quad \mathcal{S} = \int_{\mathcal{V}} \left(s - \frac{\epsilon^2}{2}|\nabla\phi|^2 \right) \mathrm{d}x, \tag{3.6}$$

where e is the specific internal energy and $s(e, \phi)$ is an entropy density. The key difference with classical thermodynamics is that $\mathcal{S}$ depends not only on ϕ, but also on its gradient. By applying the first and second laws of thermodynamics we obtain

$$\dot{\mathcal{E}} + \int_{\partial\mathcal{V}} \boldsymbol{q}\cdot\boldsymbol{n}\,\mathrm{d}a = 0, \quad \dot{\mathcal{S}} + \int_{\partial\mathcal{V}} \left(\frac{\boldsymbol{q}}{\theta} + \epsilon^2\dot{\phi}\nabla\phi \right) \boldsymbol{n}\,\mathrm{d}a \geq 0. \tag{3.7}$$

where $\partial\mathcal{V}$ is the boundary of $\mathcal{V}$. By defining a suitable expression for the specific internal energy $e(\theta, \phi)$, assuming that the latent heat is a constant and using the Coleman-Noll approach, one obtains the following model

$$\rho\, C_v \frac{\partial\theta}{\partial t} + \ell\rho h'(\phi)\frac{\partial\phi}{\partial t} = \nabla\cdot\big(k(\phi)\nabla\theta\big); \quad \omega\frac{\partial\phi}{\partial t} = \Delta\phi - \frac{W'(\phi)}{\epsilon^2} + \frac{\theta_m\ell}{H\epsilon^2}h'(\phi)\left(\frac{1}{\theta_m} - \frac{1}{\theta}\right). \tag{3.8}$$

This model is identical to Eqs. (3.5), except for the last term in the phase-field equation. To our knowledge, this model converges to the sharp interface solidification theory as $\epsilon \to 0$ only when $\theta \approx \theta_m$. However, the functional form of the last term in the phase-field equation depends on the expression of $e(\theta, \phi)$. Therefore, a judicious choice of $e(\theta, \phi)$ may lead to a model that converges, for all temperatures, to the expected sharp-interface limit as $\epsilon \to 0$. More details on this may be found in [40]. To our knowledge, deriving thermodynamically consistent solidification models that converge to the generalized Stefan problem as $\epsilon \to 0$ in the anisotropic case is an open problem.

(ii) Phase-field crystal approach to atomic scale solidification

The solidification models described up to now represent continuum descriptions of the physical process. Continuum models permit simulating long times and large systems, but sometimes fall short of incorporating fundamental physical phenomena that occurs at very small scales. Molecular dynamics [41] is an alternative approach to continuum modelling that may account for phase-transition physics at atomic length scales. The disadvantage of molecular dynamics is that simulations are restricted to very small systems and microsecond time periods at most. Recently, the phase-field crystal equation has been proposed as a model to describe two-phase systems on atomic length scales and diffusive time scales. The use of diffusive time scales allows to study much longer time intervals than those reachable with molecular dynamics simulations. The phase-field crystal equation has been employed to model multiple physical phenomena, including crystal growth in a supercooled liquid and dendritic solidification. The phase-field crystal equation can be derived from the following free-energy functional

$$\mathcal{F}[\rho] = \int_{\Omega} \left\{ \Phi(\rho) + \frac{1}{2}\left[(\Delta\rho)^2 - 2|\nabla\rho|^2 + \rho^2 \right] \right\} \mathrm{d}x, \tag{3.9}$$

where ρ represents a local atomistic density field and $\Phi(\rho) = -\frac{r}{2}\rho^2 + \frac{1}{4}\rho^4$. Here, r is the so-called undercooling coefficient [42]. By impossing mass conservation and free energy dissipation, one can derive the equation (see [43] for more details)

$$\frac{\partial \rho}{\partial t} = \Delta\left(\Phi'(\rho) + \rho + 2\Delta\rho + \Delta^2\rho \right). \tag{3.10}$$

The phase-field crystal equation has been widely studied in the computational physics [44–47] and condensed matter physics literature [48–50]. Recently, the phase-field crystal model has been generalized to account for faster dynamics [51–54].

For the computational study of the phase-field crystal equation, instead of resorting to classical finite element methods, we will illustrate here how very fast and simple algorithms can be derived using first-order accurate semi-implicit time integration schemes and fast Poisson solvers for the spatial dicretization. We begin by performing time discretization. Rearranging Eq. (3.10) and applying standard finite differences to the time derivative, we get

$$\frac{\rho_{n+1} - \rho_n}{\Delta t} = (1-r)\Delta\rho_{n+1} + \Delta(\rho_n^3) + 2\Delta^2\rho_n + \Delta^3\rho_{n+1}, \tag{3.11}$$

where ρ_n is the time discrete approximation to $\rho(x, t_n)$ and $t_n = n\Delta t$ for $n \geq 0$. Note that some of the terms on the right-hand side of Eq. (3.11) have been approximated at t_n and some others at t_{n+1}. We decided whether a linear term is approximated at t_n (explicitly) or at t_{n+1} (implicitly) based on stability considerations. Linear terms that contribute to increase the L^2 norm were approximated explicitly. This is a common approach to attain stability in time discretization schemes; see [6]. The cubic, nonlinear term was approximated explicitly to keep the algorithm linear. Basic manipulations allow us to rewrite Eq. (3.11) as

$$\left[\boldsymbol{I}_d - \Delta t(1-r)\Delta - \Delta t\Delta^3 \right] \rho_{n+1} = \rho_n + 2\Delta t\Delta^2\rho_n + \Delta t\Delta(\rho_n^3), \tag{3.12}$$

where $\boldsymbol{I}_d$ is the identity operator. What remains to be done at this point is to discretize in space, which in view of Eq. (3.12) boils down to constructing a discrete approximation of the Laplace operator. Given this situation, spatial discretization can be accomplished using a fast Poisson solver [55], which may be simply understood as a very fast implementation of a second-order finite difference method on a uniform mesh. For example, for a Poisson equation $-\Delta u + f = 0$ in two dimensions, the discretized equation at an interior node (i, j) is $4u_{i,j} - u_{i,j-1} - u_{i-1,j} - u_{i+1,j} - u_{i,j+1} = b_{ij}$, where $u_{i,j} \approx u(ih, jh)$, h is the mesh size and $b_{ij} = h^2 f(ih, jh)$. The indices i and j go from 1 to N. After collecting the equations for all the interior nodes and boundary conditions, we obtain a linear system of equations given by $\boldsymbol{K}\boldsymbol{u} = \boldsymbol{b}$. There are multiple ways to solve linear systems of equations, but they very rarely involve the use of the matrix eigenvalues. However, for the matrix $\boldsymbol{K}$ that arises from central

finite differences on a uniform mesh all eigenvalues and eigenvectors are known *a priori*. This is true for Dirichlet, Neumann and periodic boundary conditions. For conciseness, here we will only illustrate the procedure for Dirichlet boundary conditions but the method is analogous for the Neumann and periodic cases; see [55] for more details. The eigenvalues and eigenvectors of $\boldsymbol{K}$ are given by $\boldsymbol{K}\boldsymbol{v}_{kl} = \lambda_{kl}\boldsymbol{v}_{kl}$, where the component of $\boldsymbol{v}_{kl}$ corresponding to the (i,j) node is $v_{kl}^{(i,j)} = \sin(ik\pi/(N+1))\sin(jl\pi/(N+1))$ and its corresponding eigenvalue is $\lambda_{kl} = 4 - 2\left[\cos(k\pi/(N+1)) + \cos(l\pi/(N+1))\right]$. By collecting the eigenvectors $\boldsymbol{v}_{kl}$ into a matrix $\boldsymbol{S}$ and the eigenvalues into a diagonal matrix $\boldsymbol{\Lambda}$ in the usual way, we can write $\boldsymbol{K} = \boldsymbol{S}\boldsymbol{\Lambda}\boldsymbol{S}^{-1}$. Therefore, the solution to the linear system $\boldsymbol{K}\boldsymbol{u} = \boldsymbol{b}$ can be expressed as $\boldsymbol{u} = \boldsymbol{S}\boldsymbol{\Lambda}^{-1}\boldsymbol{S}^{-1}\boldsymbol{b}$. Computing the matrix $\boldsymbol{\Lambda}^{-1}$ and multiplying vectors with it is fast because $\boldsymbol{\Lambda}$ is diagonal. The matrices $\boldsymbol{S}$ and $\boldsymbol{S}^{-1}$, however, are full and even if we know them *a priori*, multiplying them with a vector requires $\mathcal{O}(N^4)$ operations[1]. The key element in the process is that multiplication of a vector with $\boldsymbol{S}$ can be interpreted as a discrete sine transform, which using the fast Fourier transform algorithm can be done in $\mathcal{O}(N^2\log_2(N^2))$ operations. By using this method, it has been shown [56] that the overall operation count is $2N^2\log_2 N$. This result is nearly optimal. Because we are considering a two-dimensional problem simply writing the solution requires N^2 operations. For Neumann boundary conditions the algorithm is very similar, but we have to use discrete cosine (rather than sine) transforms. By combining the time integration algorithm in Eq. (3.12) with the fast Poisson solver, highly efficient and surprisingly simple algorithms can be derived for the phase-field crystal equation. Below, we include a MATLAB® listing that solves the unsteady phase-field crystal equation with free flux boundary conditions and plots the solution in a few lines of code.

Listing 1: Matlab code to solve the unsteady phase-field crystal equation

```
N = 512; L=200; dx = L/(N-1); x = (0:dx:L)'; [xx,yy]= meshgrid(x',x);

it = 0; it_plot = 10; dt = .1; ntmax = 2000; r=0.5;
L1 = dt/dx^2; L2 = L1/dx^2; L3 = L2/dx^2;
LEV = (((2*cos(pi*(0:N-1)'/(N-1)))-2)*ones(1,N)); LEV = LEV + LEV';
LHS = ones(N,N) - L1*(1-r)*LEV - L3*LEV.*LEV.*LEV;
RHS = ones(N,N) + 2*L2*LEV.*LEV;

U = -.4 + 0.3*rand(N,N); hatU = dct2(U);
while it < ntmax
 if (mod(it,it_plot)==0) | (it==0);
  surf(xx,yy,U,'facecolor','interp','edgecolor','none'); colorbar; view([0,0,1]); drawnow
 end;
 it = it+1;
 hatb = RHS.*hatU + L1*LEV.*dct2(U.^3);
 hatU = hatb./LHS;
 U = idct2(hatU);
end
```

Fig. 2 shows a crystal growth simulation performed with the code provided in Listing 1, but changing the initial condition. We started the simulation with four small crystallites with different orientations surrounded by undercooled liquid; see [43]. The crystallites grow and interact with each other leaving defects at their interaction regions.

4. Liquid-gas phase transformations

Liquid-gas transformations are very important in science and engineering. Examples of physical phenomena controlled by liquid-gas transformations include vaporization, condensation, boiling and cavitation. The phase-field model that describes liquid-gas phase transformations coupled with heat transfer and flow is the so-called Navier-Stokes-Korteweg equations. A thermodynamic analysis and computational study of the Navier-Stokes-Korteweg model may be found in [57]; see also [58]. For simplicity, here, we restrict ourselves to the isothermal case [59,60]. The isothermal Navier-Stokes-Korteweg equations may be derived from an energy functional using

[1]Note that, here, N is the number of nodes per direction and the matrix $\boldsymbol{S}$ has $N^2 \times N^2$ elements

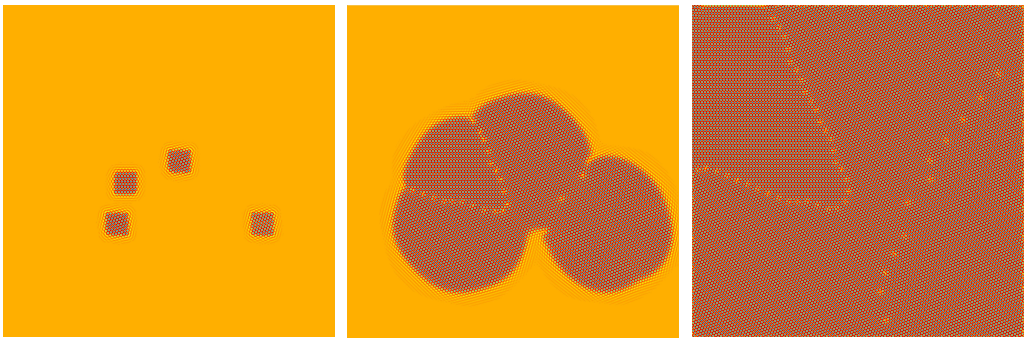

Figure 2: Simulation of the phase-field crystal equation using the code provided in Listing 1, but with an initial condition that corresponds to four small crystallites with different orientations surrounded by undercooled liquid; see [43]. The crystals grow with time, leaving remnant defects at their intersection due to their different orientations. Solution at $t = 20$, $t = 420$ and $t = 1500$.

thermomechanics. We start from the energy functional

$$\mathcal{E}[\rho, \nabla\rho, \boldsymbol{u}] = \int_{\mathcal{P}_t} \left(\Psi + \frac{1}{2}\rho|\boldsymbol{u}|^2 \right) \mathrm{d}x, \tag{4.1}$$

where $\mathcal{P}_t$ is a set of material particles in the current configuration, $\Psi = \hat{\Psi}(\rho, \nabla\rho)$, ρ is the fluid density and $\boldsymbol{u}$ is the fluid velocity. Then, we use mass, linear momentum and angular momentum balance laws

$$\dot{\rho} + \rho\,\nabla\cdot\boldsymbol{u} = 0, \quad \rho\,\dot{\boldsymbol{u}} = \nabla\cdot\,\boldsymbol{T}, \quad \boldsymbol{T} = \boldsymbol{T}^T, \tag{4.2}$$

where $\dot{\rho} = \frac{\partial\rho}{\partial t} + \boldsymbol{u}\cdot\nabla\rho$ denotes the material derivative of the fluid density and $\boldsymbol{T} = \hat{\boldsymbol{T}}(\boldsymbol{L}, \rho, \nabla\rho, \mu)$ is the Cauchy stress tensor. Here, $\boldsymbol{L} = \frac{1}{2}(\nabla\boldsymbol{u} + \nabla\boldsymbol{u}^T)$ and $\mu = \frac{\partial\hat{\Psi}}{\partial\rho} - \nabla\cdot\left(\frac{\partial\hat{\Psi}}{\partial\nabla\rho}\right)$. By imposing the dissipation law $\dot{\mathcal{E}} = -\mathcal{D}(\mathcal{P}_t) + \mathcal{B}(\partial\mathcal{P}_t)$, with $\mathcal{D}(\mathcal{P}_t) \geq 0$, we can determine a suitable form of the stress tensor $\boldsymbol{T}$. Using standard continuum mechanics, the chain rule, the relation $(\nabla\rho)^{\cdot} = \nabla\dot{\rho} - \nabla\boldsymbol{u}\nabla\rho$ and the balance laws we can show that

$$\dot{\mathcal{E}} = \int_{\mathcal{P}_t} \left(-\frac{\partial\hat{\Psi}}{\partial\rho}\rho\nabla\cdot\boldsymbol{u} + \frac{\partial\hat{\Psi}}{\partial\nabla\rho}\nabla\dot{\rho} - \frac{\partial\hat{\Psi}}{\partial\nabla\rho}\cdot\nabla\boldsymbol{u}\nabla\rho + \Psi\nabla\cdot\boldsymbol{u} + \boldsymbol{u}\cdot\nabla\cdot\boldsymbol{T} \right) \mathrm{d}x. \tag{4.3}$$

Integrating by parts and using the relation $\frac{\partial\hat{\Psi}}{\partial\nabla\rho}\cdot\nabla\boldsymbol{u}\nabla\rho = \frac{\partial\hat{\Psi}}{\partial\nabla\rho}\otimes\nabla\rho : \nabla\boldsymbol{u}$, one can derive

$$\dot{\mathcal{E}} = \int_{\mathcal{P}_t} \left((\Psi - \rho\mu)\boldsymbol{I} - \frac{\partial\hat{\Psi}}{\partial\nabla\rho}\otimes\nabla\rho - \boldsymbol{T} \right) : \nabla\boldsymbol{u}\,\mathrm{d}x + \int_{\partial\mathcal{P}_t} \left(\dot{\rho}\frac{\partial\hat{\Psi}}{\partial\nabla\rho}\cdot\boldsymbol{n} + \boldsymbol{u}\cdot\,\boldsymbol{T}\boldsymbol{n} \right) \mathrm{d}a, \tag{4.4}$$

where $\boldsymbol{I}$ is the identity tensor. Eq. (4.4) allows to identify $\mathcal{D}(\mathcal{P}_t)$ and $\mathcal{B}(\partial\mathcal{P}_t)$ as

$$\mathcal{D}(\mathcal{P}_t) = \int_{\mathcal{P}_t} \left((\rho\mu - \Psi)\boldsymbol{I} + \frac{\partial\hat{\Psi}}{\partial\nabla\rho}\otimes\nabla\rho + \boldsymbol{T} \right) : \nabla\boldsymbol{u}\,\mathrm{d}x, \tag{4.5}$$

$$\mathcal{B}(\partial\mathcal{P}_t) = \int_{\partial\mathcal{P}_t} \left(\dot{\rho}\frac{\partial\hat{\Psi}}{\partial\nabla\rho}\cdot\boldsymbol{n} + \boldsymbol{u}\cdot\,\boldsymbol{T}\boldsymbol{n} \right) \mathrm{d}a. \tag{4.6}$$

If we now use frame invariance arguments to show that $\frac{\partial\hat{\Psi}}{\partial\nabla\rho}\otimes\nabla\rho$ is a symmetric tensor and impose $\mathcal{D}(\mathcal{P}_t) \geq 0$ for all conceivable process, we obtain a possible expression for the Cauchy stress tensor given by

$$(\rho\mu - \Psi)\boldsymbol{I} + \frac{\partial\hat{\Psi}}{\partial\nabla\rho}\otimes\nabla\rho + \boldsymbol{T} = 2\overline{\mu}\boldsymbol{L} + \overline{\lambda}\nabla\cdot\boldsymbol{u}\boldsymbol{I}, \tag{4.7}$$

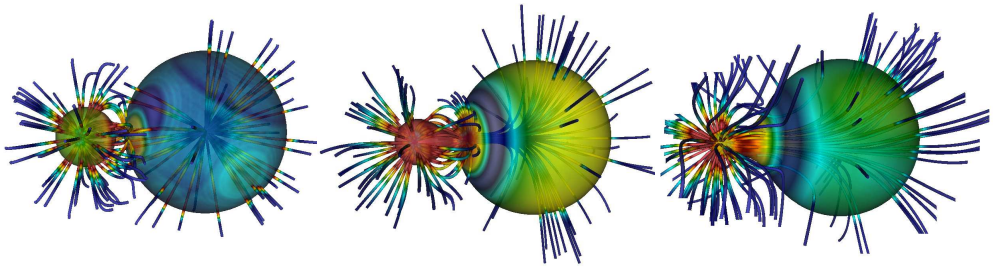

Figure 3: Three-dimensional simulation of the Navier-Stokes-Korteweg equations. Two gas bubbles which are initially close to each other coalesce into a single one. The plot also shows streamlines. The color scale indicates velocity magnitude.

where $\overline{\mu}$ and $\overline{\lambda}$ are viscosity coefficients satisfying $\overline{\mu} \geq 0$ and $\frac{2\overline{\mu}}{3} + \overline{\lambda} \geq 0$. By using the expression of $\hat{\Psi}$ for a Van der Vaals fluid

$$\hat{\Psi} = \mathcal{W}(\rho) + \frac{\lambda}{2}|\nabla\rho|^2, \quad \text{with} \quad \mathcal{W}(\rho) = R\,\theta\rho\log\left(\frac{\rho}{b-\rho}\right) - a\rho, \tag{4.8}$$

we obtain

$$\boldsymbol{T} = \left(-p + \frac{1}{2}\lambda|\nabla\rho|^2 + \lambda\rho\Delta\rho\right)\boldsymbol{I} - \lambda\nabla\rho\otimes\nabla\rho + 2\overline{\mu}\boldsymbol{L} + \overline{\lambda}\nabla\cdot\boldsymbol{u}\boldsymbol{I}, \tag{4.9}$$

where $p = \rho\,\mathcal{W}'(\rho) - \mathcal{W}(\rho)$ is the thermodynamic pressure, θ is the (constant) temperature and a, b are constants that define the fluid's equation of state. Multiple algorithms have been used for the solution of the Navier-Stokes-Korteweg equations, including discontinuous Galerkin methods [58] and isogeometric analysis [59]. Fig. 3 shows a simulation performed using the isogeometric discretization proposed in [59]. The computation shows how two vapor bubbles which are close to each other coalesce into a single one.

5. Solid-solid phase transformations

Solid-solid phase transformations usually manifest themselves as changes in the material's microstructure. Material's microstructures are structural and compositional inhomogeneities. They may consist of grains of different orientations, domains of phases with different compositions or domains of different structural variants. Material's microstructures usually arrange in space, with characteristic sizes in the order of microns. Understanding microstructure evolution is crucial in materials science and engineering because the microstructure has a strong impact on the macroscale physical properties of a material. During microstructure evolution the interfaces that separate different domains move in a very complex way. Thus, not surprisingly, the phase-field method has attracted a lot of attention in materials science research [61,62].

(a) Martensitic transformations

Martensitic transformations are diffusionless, first-order, solid-solid transformations. Atomistic simulations (see, e.g., [63]) have been used to explore systems of size up to $\sim 10\,\mathrm{nm}$ for a few nanoseconds. The sharp-interface approach has also been utilized [64]. In recent years, the phase-field method has established itself as a powerful tool to model martensitic transformations. Multiple models have been proposed for isothermal [65] and thermally-coupled systems [66]. Here, we review and extend to the large deformation regime one of the representative models [65]. To introduce the model we consider a set of material points P_0, which may be understood as the initial configuration of the solid. We consider the usual mapping $\boldsymbol{\varphi}$ which takes P_0 into the current configuration. The displacement field is defined as $\boldsymbol{d} = \boldsymbol{\varphi} - \boldsymbol{I}_d$, where $\boldsymbol{I}_d$ represents the identity mapping. The deformation gradient and the Cauchy-Green tensor are defined, respectively, as $\boldsymbol{F} = \nabla\boldsymbol{\varphi}$ and $\boldsymbol{C} = \boldsymbol{F}\boldsymbol{F}^T$. The model considers two martensitic variants represented by the phase

fields ϕ_1 and ϕ_2 which take values between 0 and 1. The austenite phase is located where $\phi_1 = \phi_2 = 0$. The free-energy of the system may be written as

$$\Psi = \int_{P_0} \left\{ w^e\left(\boldsymbol{C}, \phi_1, \phi_2\right) + \psi^g\left(\phi_1, \nabla\phi_1, \phi_2, \nabla\phi_2\right) + \frac{1}{2}\rho_0 |\dot{\boldsymbol{d}}|^2 \right\} \mathrm{d}x, \tag{5.1}$$

where w^e represents the composition-dependent elastic energy, ψ^g denotes the Ginzburg-Landau energy and $\frac{1}{2}\rho_0|\dot{\boldsymbol{d}}|^2$ accounts for the kinetic energy. We now use conservation of linear momentum and mass balance laws for the martensitic variants

$$\rho_0 \ddot{\boldsymbol{d}} - \nabla \cdot \boldsymbol{P} = 0, \quad \dot{\phi}_1 + R_1 = 0, \quad \dot{\phi}_2 + R_2 = 0, \tag{5.2}$$

where $\boldsymbol{P}$ is the first Piola-Kirchhoff stress tensor. We postulate the dissipation law $\dot{\Psi} = \mathcal{W}(P_0) - \mathcal{D}(P_0)$, where $\mathcal{D}(P_0) \geq 0$ for all solutions to the balance laws. By taking the time derivative of the free-energy, integrating by parts and using the balance laws, we obtain

$$\begin{aligned} \dot{\Psi} \quad = \quad & \int_{P_0} \left\{ \frac{\partial w^e}{\partial \boldsymbol{C}} \dot{\boldsymbol{C}} - R_1 \frac{\partial w^e}{\partial \phi_1} - R_2 \frac{\partial w^e}{\partial \phi_2} + \mu_1 \dot{\phi}_1 + \mu_2 \dot{\phi}_2 - \boldsymbol{P} : \nabla \dot{\boldsymbol{d}} \right\} \mathrm{d}x \\ & + \int_{\partial P_0} \left\{ \frac{\partial \psi^g}{\partial \nabla \phi_1} \cdot \boldsymbol{n} \dot{\phi}_1 + \frac{\partial \psi^g}{\partial \nabla \phi_2} \cdot \boldsymbol{n} \dot{\phi}_2 + \boldsymbol{P}\boldsymbol{n} \cdot \dot{\boldsymbol{d}} \right\} \mathrm{d}a, \end{aligned} \tag{5.3}$$

where $\mu_1 = \frac{\partial \psi^g}{\partial \phi_1} - \nabla \cdot \left(\frac{\partial \psi^g}{\partial \nabla \phi_1} \right)$ and $\mu_2 = \frac{\partial \psi^g}{\partial \phi_2} - \nabla \cdot \left(\frac{\partial \psi^g}{\partial \nabla \phi_2} \right)$ are referred to as chemical potentials. Using the identities $\nabla \dot{\boldsymbol{d}} = \dot{\boldsymbol{F}}$ and $\boldsymbol{P} : \dot{\boldsymbol{F}} = \frac{1}{2}\boldsymbol{S} : \dot{\boldsymbol{C}}$ where $\boldsymbol{P} = \boldsymbol{F}\boldsymbol{S}$, we obtain

$$\begin{aligned} \dot{\Psi} \quad = \quad & \int_{P_0} \left\{ \left(\frac{\partial w^e}{\partial \boldsymbol{C}} - \frac{1}{2}\boldsymbol{S} \right) : \dot{\boldsymbol{C}} - R_1 \left(\frac{\partial w^e}{\partial \phi_1} + \mu_1 \right) - R_2 \left(\frac{\partial w^e}{\partial \phi_2} + \mu_2 \right) \right\} \mathrm{d}x \\ + \quad & \int_{\partial P_0} \left\{ \frac{\partial \psi^g}{\partial \nabla \phi_1} \cdot \boldsymbol{n} \dot{\phi}_1 + \frac{\partial \psi^g}{\partial \nabla \phi_2} \cdot \boldsymbol{n} \dot{\phi}_2 + \boldsymbol{P}\boldsymbol{n} \cdot \dot{\boldsymbol{d}} \right\} \mathrm{d}a. \end{aligned} \tag{5.4}$$

Therefore, we can take

$$\boldsymbol{S} = 2\frac{\partial w^e}{\partial \boldsymbol{C}}, \quad R_1 = m_1 \left(\frac{\partial w^e}{\partial \phi_1} + \mu_1 \right), \quad R_2 = m_2 \left(\frac{\partial w^e}{\partial \phi_2} + \mu_2 \right), \tag{5.5}$$

with $m_1 \geq 0$ and $m_2 \geq 0$. This model is usually employed in the small deformation regime and assuming quasi-static mechanical equilibrium. Under these assumptions, common expressions for the free energy are

$$w^e\left(\boldsymbol{\varepsilon}, \phi_1, \phi_2\right) = \frac{1}{2} \left[\varepsilon_{ij} - \varepsilon^0_{ij}(\phi_1, \phi_2) \right] \mathbb{C}_{ijkl}(\phi_1, \phi_2) \left[\varepsilon_{kl} - \varepsilon^0_{kl}(\phi_1, \phi_2) \right], \tag{5.6}$$

where repeated indices indicate summation, $\boldsymbol{\varepsilon} = \frac{1}{2}(\nabla \boldsymbol{d} + \nabla \boldsymbol{d}^T)$ is the infinitesimal strain tensor and $\mathbb{C}(\phi_1, \phi_2)$ is the elasticity matrix that varies linearly between the austenitic matrix and the martensite phase, i.e., $\mathbb{C}(\phi_1, \phi_2) = \mathbb{C}_A + \phi_1 \left(\mathbb{C}_M - \mathbb{C}_A \right) + \phi_2 \left(\mathbb{C}_M - \mathbb{C}_A \right)$. Here, $\mathbb{C}_M$ and $\mathbb{C}_A$ represent, respectively, the martensite and austenite elasticity matrices. The transformation-induced eigenstrains are defined as $\boldsymbol{\varepsilon}^0(\phi_1, \phi_2) = \phi_1 \boldsymbol{\varepsilon}^0_1 + \phi_2 \boldsymbol{\varepsilon}^0_2$. The Ginzburg-Laundau free energy is defined as

$$\psi^g(\phi_1, \nabla\phi_1, \phi_2, \nabla\phi_2) = \kappa_s \frac{G}{L} f(\phi_1, \phi_2) + \frac{1}{2}\kappa_g G L \left(|\nabla\phi_1|^2 + |\nabla\phi_2|^2 \right), \tag{5.7}$$

where

$$f(\phi_1, \phi_2) = 1 + \frac{\alpha}{2}\left(\phi_1^2 + \phi_2^2\right) - \frac{\beta}{3}\left(\phi_1^3 + \phi_2^3\right) + \frac{\gamma}{4}\left(\phi_1^2 + \phi_2^2\right)^2. \tag{5.8}$$

Here, κ_s, κ_g, α, β and γ are constants. In this simplified setting, the governing equations may be written as

$$\nabla \cdot \boldsymbol{\sigma} = 0, \quad \frac{\partial \phi_1}{\partial t} + m_1 \left(\frac{\partial w^e}{\partial \phi_1} + \mu_1 \right) = 0, \quad \frac{\partial \phi_2}{\partial t} + m_2 \left(\frac{\partial w^e}{\partial \phi_2} + \mu_2 \right) = 0, \tag{5.9}$$

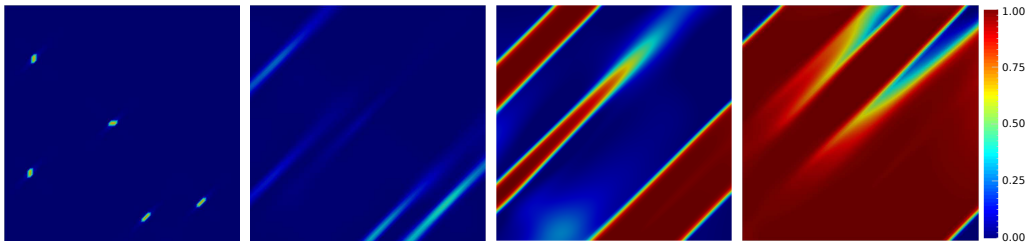

Figure 4: Numerical simulation of Eqs. (5.9). The color scale corresponds to ϕ_1. We start the simulation with five random seeds of the martensitic variant ϕ_1. The variant ϕ_2 is assumed to be zero. The parameters are taken as in [67].

where $\sigma_{ij} = \mathbb{C}_{ijkl}(\phi_1, \phi_2)[\varepsilon_{kl} - \varepsilon^0_{kl}(\phi_1, \phi_2)]$. Eqs. (5.9) can be discretized, e.g., using finite differences in time and finite elements in space. Fig. 4 shows a simulation using the finite element code provided in [67].

(b) Grain growth

Most materials of engineering interest are composed by multiple grains with different crystallographic orientations. Some grains grow at the expense of others, leading to an evolution of the material's microstructure. Grain growth has been studied using sharp-interface methods [68], but the algorithmic tracking of the interfaces becomes very cumbersome for a large number of grains. Phase-field models have grown significantly since the early work by Chen and Yang [69], which was later improved in [70]. The model is derived from the free energy

$$\mathcal{F}[\eta_1, \eta_2, \ldots, \eta_N] = \int_{\mathcal{V}} \left\{ f(\eta_1, \eta_2, \cdots, \eta_N) + \sum_{i=1}^{N} \frac{\kappa_i}{2} |\nabla \eta_i|^2 \right\} \mathrm{d}x, \tag{5.10}$$

where

$$f(\eta_1, \eta_2, \cdots, \eta_N) = \sum_{i=1}^{N} \left[-\frac{\alpha}{2}\eta_i^2 + \frac{\beta}{4}\eta_i^4 \right] + \gamma \sum_{i=1}^{N} \sum_{\substack{j=1 \\ j \neq i}}^{N} \eta_i^2 \eta_j^2. \tag{5.11}$$

By using the standard themomechanics approach, we can derive the governing equations

$$\frac{\partial \eta_i}{\partial t} = -L_i \frac{\delta \mathcal{F}}{\delta \eta_i}, \quad \text{where} \quad \frac{\delta \mathcal{F}}{\delta \eta_i} = -\alpha \eta_i + \beta \eta_i^3 + 2\gamma\, \eta_i \sum_{\substack{j=1 \\ j \neq i}}^{N} \eta_j^2 - \kappa_i \Delta \eta_i \tag{5.12}$$

is the variational derivative of $\mathcal{F}$ and the L_i's are positive constants. Fig. 5 shows a simulation of Eqs. (5.12) for 25 grains ($N = 25$) using the finite-difference code provided in [67].

6. Adaptive mesh refinement

Phase-field models have significant advantages with respect to sharp-interface methods. They avoid interface tracking, which is very difficult when many interface types are present; they can easily handle topological changes; and they permit to couple interface motion with bulk physics in a straightforward manner. However, when computations are performed on uniform meshes they may be suboptimal from the point of view of computational cost even if they are simpler formulations. For example, if we want to study solidification of a pure material in three dimensions using a sharp-interface method, the energy balance equation needs to be solved in the volume of the pure phases, but the interface motion remains as a 2D problem. When we introduce the phase-field formulation, the interface problem becomes 3D. Because the phase-field is approximately constant away from the interface, it is possible to concentrate small elements in the interfacial area and use very coarse meshes in the bulk areas, somehow retrieving a quasi-2D

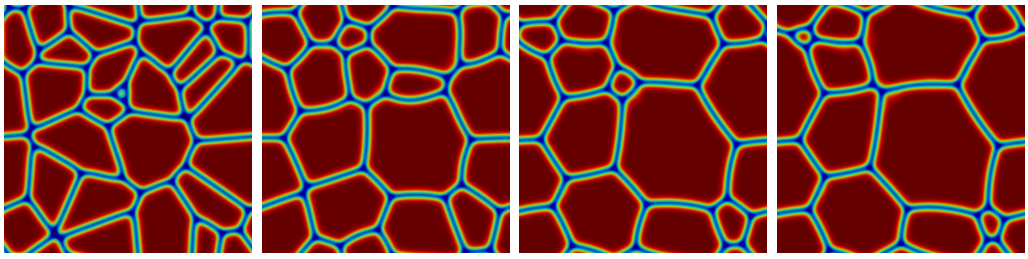

Figure 5: Simulation of grain growth. We used 25 grains with different crystallographic orientations. The parameters were selected as in [67].

problem that enjoys all the advantages of the phase-field method. Adaptive mesh refinement is the ideal mathematical tool to do this is.

Adaptive mesh refinement can be done using simple, heuristic criteria, such as for example, refining the regions where the phase-field is far from the pure phase values or where the gradient of the phase-field is large. These approaches have proven very useful (see [71–73]), but they may lead to inaccurate solutions on coarse meshes. A rigorous approach for adaptive mesh refinement is that provided by *a posteriori* error estimates. The simplest and most widely known estimator in this category is the Zienkiewicz-Zhu gradient-recovery method [74], which can be used for the spatial discretization in a method-of-lines approach. Adaptive mesh refinement was used in 2D computational phase-field modelling almost since its inception [75]. More recently, the approach was extended to 3D and complex geometries using a hierarchical approach to local refinement [71]. In this reference, the adaptive approach was implemented in a dynamic context, so that the mesh evolves in time to resolve the moving interface. The total number of elements in a representative simulation with the adaptive approach was approximately 13% of the number of elements that would be required to attain the same spatial resolution at the interface with a uniform mesh.

Time step adaptivity has also been shown to be crucially important in some phase-field models. For example, for the Cahn-Hilliard equation, which describes phase separation of immiscible fluids, it has been reported that keeping time accuracy approximately constant throughout a simulation may require variations in the time step of up to six orders of magnitude [76]. Time step adaptivity can be performed using classical approaches from the ordinary differential equations literature [77]. A commonly used method consists of computing each time step using a lower order and a higher order time stepping scheme. The difference between the lower order and the higher order approximation is an error estimate that can be used to adapt the time step [76]. While this approach requires computing each time step twice, it leads to dramatic savings when the adapted time step spans several orders of magnitude.

Finally, the most rigorous approach to adaptivity is based on space-time a posteriori error estimates. The estimates are usually derived using residual-based approaches [78] or resorting to dual problems [79].

Data Accessibility. The article has no additional data.

Authors' Contributions. HG conceived and designed the study and drafted the manuscript. HG, MB and AM carried out the experiments. All auhtors read and approved the manuscript.

Competing Interests. The authors declare that they have no competing interests.

Funding. The concepts and results reviewed in this work were partially funded by the NSF Research Grant CBET-1805817.

References

1. T. H. Colding and W. P. Minicozzi, "Generic mean curvature flow i; generic singularities," *Annals of mathematics*, vol. 175, pp. 755–833, 2012.

2. S. R. Idelsohn, M. A. Storti, and L. A. Crivelli, "Numerical methods in phase-change problems," *Archives of Computational Methods in Engineering*, vol. 1, no. 1, pp. 49–74, 1994.
3. J. A. Sethian, *Level set methods and fast marching methods: evolving interfaces in computational geometry, fluid mechanics, computer vision, and materials science*, vol. 3. Cambridge university press, 1999.
4. S. Osher and J. A. Sethian, "Fronts propagating with curvature-dependent speed: algorithms based on hamilton-jacobi formulations," *Journal of computational physics*, vol. 79, no. 1, pp. 12–49, 1988.
5. S. Osher and R. Fedkiw, *Level set methods and dynamic implicit surfaces*, vol. 153. Springer Science & Business Media, 2006.
6. H. Gomez and K. G. van der Zee, "Computational phase-field modeling," *Encyclopedia of Computational Mechanics Second Edition*, pp. 1–35, 2018.
7. D. M. Anderson, G. B. McFadden, and A. A. Wheeler, "Diffuse-interface methods in fluid mechanics," *Annual review of fluid mechanics*, vol. 30, no. 1, pp. 139–165, 1998.
8. H. Emmerich, *The diffuse interface approach in materials science: thermodynamic concepts and applications of phase-field models*, vol. 73. Springer Science & Business Media, 2003.
9. N. Provatas and K. Elder, *Phase-field methods in materials science and engineering*. John Wiley & Sons, 2011.
10. L.-Q. Chen, "Phase-field models for microstructure evolution," *Annual Review of Materials Science*, vol. 32, pp. 113–140, 2002.
11. C. Hesch, A. Gil, R. Ortigosa, M. Dittmann, C. Bilgen, P. Betsch, M. Franke, A. Janz, and K. Weinberg, "A framework for polyconvex large strain phase-field methods to fracture," *Computer Methods in Applied Mechanics and Engineering*, vol. 317, pp. 649–683, 2017.
12. M. Ambati, T. Gerasimov, and L. De Lorenzis, "A review on phase-field models of brittle fracture and a new fast hybrid formulation," *Computational Mechanics*, vol. 55, no. 2, pp. 383–405, 2015.
13. C. Miehe, F. Welschinger, and M. Hofacker, "Thermodynamically consistent phase-field models of fracture: Variational principles and multi-field fe implementations," *International Journal for Numerical Methods in Engineering*, vol. 83, no. 10, pp. 1273–1311, 2010.
14. M. J. Borden, C. V. Verhoosel, M. A. Scott, T. J. Hughes, and C. M. Landis, "A phase-field description of dynamic brittle fracture," *Computer Methods in Applied Mechanics and Engineering*, vol. 217, pp. 77–95, 2012.
15. J. Kiendl, M. Ambati, L. De Lorenzis, H. Gomez, and A. Reali, "Phase-field description of brittle fracture in plates and shells," *Computer Methods in Applied Mechanics and Engineering*, vol. 312, pp. 374–394, 2016.
16. J. Bueno, C. Bona-Casas, Y. Bazilevs, and H. Gomez, "Interaction of complex fluids and solids: theory, algorithms and application to phase-change-driven implosion," *Computational Mechanics*, vol. 55, no. 6, pp. 1105–1118, 2015.
17. L. Cueto-Felgueroso and R. Juanes, "A phase-field model of two-phase hele-shaw flow," *Journal of Fluid Mechanics*, vol. 758, pp. 522–552, 2014.
18. S. Aland, J. Lowengrub, and A. Voigt, "Two-phase flow in complex geometries: A diffuse domain approach," *Computer modeling in engineering & sciences: CMES*, vol. 57, no. 1, p. 77, 2010.
19. Y. Xie, O. Wodo, and B. Ganapathysubramanian, "Incompressible two-phase flow: Diffuse interface approach for large density ratios, grid resolution study, and 3d patterned substrate wetting problem," *Computers & Fluids*, vol. 141, pp. 223–234, 2016.
20. F. Campelo and A. Hernandez-Machado, "Dynamic model and stationary shapes of fluid vesicles," *The European Physical Journal E*, vol. 20, no. 1, pp. 37–45, 2006.
21. Q. Du, C. Liu, and X. Wang, "A phase field approach in the numerical study of the elastic bending energy for vesicle membranes," *Journal of Computational Physics*, vol. 198, no. 2, pp. 450–468, 2004.
22. G. Lorenzo, M. A. Scott, K. Tew, T. J. Hughes, Y. J. Zhang, L. Liu, G. Vilanova, and H. Gomez, "Tissue-scale, personalized modeling and simulation of prostate cancer growth," *Proceedings of the National Academy of Sciences*, p. 201615791, 2016.
23. G. Vilanova, I. Colominas, and H. Gomez, "A mathematical model of tumour angiogenesis: growth, regression and regrowth," *Journal of The Royal Society Interface*, vol. 14, no. 126, p. 20160918, 2017.

24. G. Vilanova, M. Burés, I. Colominas, and H. Gomez, "Computational modelling suggests complex interactions between interstitial flow and tumour angiogenesis," *Journal of The Royal Society Interface*, vol. 15, no. 146, p. 20180415, 2018.
25. D. Mokbel, H. Abels, and S. Aland, "A phase-field model for fluid-structure-interaction," *arXiv preprint arXiv:1803.02354*, 2018.
26. D. Shao, W.-J. Rappel, and H. Levine, "Computational model for cell morphodynamics," *Physical review letters*, vol. 105, no. 10, p. 108104, 2010.
27. A. Moure and H. Gomez, "Phase-field model of cellular migration: Three-dimensional simulations in fibrous networks," *Computer Methods in Applied Mechanics and Engineering*, vol. 320, pp. 162–197, 2017.
28. W. J. Boettinger, J. A. Warren, C. Beckermann, and A. Karma, "Phase-field simulation of solidification," *Annual review of materials research*, vol. 32, no. 1, pp. 163–194, 2002.
29. T. Ilmanen *et al.*, "Convergence of the allen-cahn equation to brakkeâĂŹs motion by mean curvature," *J. Differential Geom*, vol. 38, no. 2, pp. 417–461, 1993.
30. X. Feng and A. Prohl, "Numerical analysis of the allen-cahn equation and approximation for mean curvature flows," *Numerische Mathematik*, vol. 94, no. 1, pp. 33–65, 2003.
31. S. M. Allen and J. W. Cahn, "A microscopic theory for antiphase boundary motion and its application to antiphase domain coarsening," *Acta Metallurgica*, vol. 27, no. 6, pp. 1085–1095, 1979.
32. A. J. Bray, "Theory of phase-ordering kinetics," *Advances in Physics*, vol. 51, no. 2, pp. 481–587, 2002.
33. B. D. Coleman and W. Noll, "The thermodynamics of elastic materials with heat conduction and viscosity," *Archive for Rational Mechanics and Analysis*, vol. 13, no. 1, pp. 167–178, 1963.
34. C. Truesdell and W. Noll, "The non-linear field theories of mechanics," in *The non-linear field theories of mechanics*, pp. 1–579, Springer, 2004.
35. M. C. Flemings, "Solidification processing," *Metallurgical Transactions*, vol. 5, pp. 2121–2134, Oct 1974.
36. W. Kurz and D. J. Fisher, *Fundamentals of solidification*, vol. 1.
trans tech publications Aedermannsdorf, Switzerland, 1986.
37. T. J. Hughes, J. A. Cottrell, and Y. Bazilevs, "Isogeometric analysis: Cad, finite elements, nurbs, exact geometry and mesh refinement," *Computer methods in applied mechanics and engineering*, vol. 194, no. 39-41, pp. 4135–4195, 2005.
38. S.-L. Wang, R. Sekerka, A. Wheeler, B. Murray, S. Coriell, R. Braun, and G. McFadden, "Thermodynamically-consistent phase-field models for solidification," *Physica D: Nonlinear Phenomena*, vol. 69, no. 1-2, pp. 189–200, 1993.
39. O. Penrose and P. C. Fife, "Thermodynamically consistent models of phase-field type for the kinetic of phase transitions," *Physica D: Nonlinear Phenomena*, vol. 43, no. 1, pp. 44–62, 1990.
40. A. Karma and W.-J. Rappel, "Phase-field method for computationally efficient modeling of solidification with arbitrary interface kinetics," *Physical review E*, vol. 53, no. 4, p. R3017, 1996.
41. J. M. Haile, *Molecular dynamics simulation: elementary methods*, vol. 1.
Wiley New York, 1992.
42. U. Thiele, A. J. Archer, M. J. Robbins, H. Gomez, and E. Knobloch, "Localized states in the conserved swift-hohenberg equation with cubic nonlinearity," *Physical Review E*, vol. 87, no. 4, p. 042915, 2013.
43. H. Gomez and X. Nogueira, "An unconditionally energy-stable method for the phase field crystal equation," *Computer Methods in Applied Mechanics and Engineering*, vol. 249, pp. 52–61, 2012.
44. J. Shin, H. G. Lee, and J.-Y. Lee, "First and second order numerical methods based on a new convex splitting for phase-field crystal equation," *Journal of Computational Physics*, vol. 327, pp. 519 – 542, 2016.
45. Z. Zhang, Y. Ma, and Z. Qiao, "An adaptive time-stepping strategy for solving the phase field crystal model," *Journal of Computational Physics*, vol. 249, pp. 204 – 215, 2013.
46. Z. Guan, V. Heinonen, J. Lowengrub, C. Wang, and S. M. Wise, "An energy stable, hexagonal finite difference scheme for the 2d phase field crystal amplitude equations," *Journal of Computational Physics*, vol. 321, pp. 1026 – 1054, 2016.
47. J. Zhao, X. Yang, J. Shen, and Q. Wang, "A decoupled energy stable scheme for a hydrodynamic phase-field model of mixtures of nematic liquid crystals and viscous fluids," *Journal of Computational Physics*, vol. 305, pp. 539 – 556, 2016.

48. K. Elder and M. Grant, "Modeling elastic and plastic deformations in nonequilibrium processing using phase field crystals," *Physical Review E*, vol. 70, no. 5, p. 051605, 2004.
49. K. Elder, M. Katakowski, M. Haataja, and M. Grant, "Modeling elasticity in crystal growth," *Physical review letters*, vol. 88, no. 24, p. 245701, 2002.
50. K. Elder, N. Provatas, J. Berry, P. Stefanovic, and M. Grant, "Phase-field crystal modeling and classical density functional theory of freezing," *Physical Review B*, vol. 75, no. 6, p. 064107, 2007.
51. P. Stefanovic, M. Haataja, and N. Provatas, "Phase-field crystals with elastic interactions," *Physical review letters*, vol. 96, no. 22, p. 225504, 2006.
52. P. Stefanovic, M. Haataja, and N. Provatas, "Phase field crystal study of deformation and plasticity in nanocrystalline materials," *Physical Review E*, vol. 80, no. 4, p. 046107, 2009.
53. P. Galenko and S. Sobolev, "Local nonequilibrium effect on undercooling in rapid solidification of alloys," *Physical Review E*, vol. 55, no. 1, p. 343, 1997.
54. P. Galenko, D. Danilov, and V. Lebedev, "Phase-field-crystal and swift-hohenberg equations with fast dynamics," *Physical Review E*, vol. 79, no. 5, p. 051110, 2009.
55. G. Strang, *Introduction to applied mathematics*, vol. 16.
Wellesley-Cambridge Press Wellesley, MA, 1986.
56. P. N. Swarztrauber, "The methods of cyclic reduction, fourier analysis and the facr algorithm for the discrete solution of poisson's equation on a rectangle," *Siam Review*, vol. 19, no. 3, pp. 490–501, 1977.
57. J. Liu, C. M. Landis, H. Gomez, and T. J. Hughes, "Liquid–vapor phase transition: Thermomechanical theory, entropy stable numerical formulation, and boiling simulations," *Computer Methods in Applied Mechanics and Engineering*, vol. 297, pp. 476–553, 2015.
58. L. Tian, Y. Xu, J. Kuerten, and J. J. van der Vegt, "A local discontinuous galerkin method for the (non)-isothermal navier–stokes–korteweg equations," *Journal of computational physics*, vol. 295, pp. 685–714, 2015.
59. H. Gomez, T. J. Hughes, X. Nogueira, and V. M. Calo, "Isogeometric analysis of the isothermal navier–stokes–korteweg equations," *Computer Methods in Applied Mechanics and Engineering*, vol. 199, no. 25-28, pp. 1828–1840, 2010.
60. J. Liu, H. Gomez, J. A. Evans, T. J. Hughes, and C. M. Landis, "Functional entropy variables: a new methodology for deriving thermodynamically consistent algorithms for complex fluids, with particular reference to the isothermal navier–stokes–korteweg equations," *Journal of Computational Physics*, vol. 248, pp. 47–86, 2013.
61. L.-Q. Chen, "Phase-field models for microstructure evolution," *Annual review of materials research*, vol. 32, no. 1, pp. 113–140, 2002.
62. M. Mamivand, M. A. Zaeem, and H. El Kadiri, "A review on phase field modeling of martensitic phase transformation," *Computational Materials Science*, vol. 77, pp. 304–311, 2013.
63. L. Sandoval and H. M. Urbassek, "Transformation pathways in the solid-solid phase transitions of iron nanowires," *Applied Physics Letters*, vol. 95, no. 19, p. 191909, 2009.
64. M. Cherkaoui and M. Berveiller, "Micromechanical modeling of the martensitic transformation induced plasticity in steels," *Smart materials and structures*, vol. 9, no. 5, p. 592, 2000.
65. R. Schmitt, R. Müller, C. Kuhn, and H. M. Urbassek, "A phase field approach for multivariant martensitic transformations of stable and metastable phases," *Archive of Applied Mechanics*, vol. 83, no. 6, pp. 849–859, 2013.
66. R. P. Dhote, H. Gomez, R. N. Melnik, and J. Zu, "Shape memory alloy nanostructures with coupled dynamic thermo-mechanical effects," *Computer Physics Communications*, vol. 192, pp. 48–53, 2015.
67. S. B. Biner, *Programming phase-field modeling*.
Springer, 2017.
68. F. Wakai, N. Enomoto, and H. Ogawa, "Three-dimensional microstructural evolution in ideal grain growth-general statistics," *Acta Materialia*, vol. 48, no. 6, pp. 1297–1311, 2000.
69. L.-Q. Chen and W. Yang, "Computer simulation of the domain dynamics of a quenched system with a large number of nonconserved order parameters: The grain-growth kinetics," *Physical Review B*, vol. 50, no. 21, p. 15752, 1994.
70. D. Fan and L.-Q. Chen, "Computer simulation of grain growth using a continuum field model," *Acta Materialia*, vol. 45, no. 2, pp. 611–622, 1997.
71. G. Lorenzo, M. Scott, K. Tew, T. Hughes, and H. Gomez, "Hierarchically refined and coarsened splines for moving interface problems, with particular application to phase-field models of

prostate tumor growth," *Computer Methods in Applied Mechanics and Engineering*, vol. 319, pp. 515–548, 2017.
72. N. Provatas, M. Greenwood, B. Athreya, N. Goldenfeld, and J. Dantzig, "Multiscale modeling of solidification: Phase-field methods to adaptive mesh refinement," *International Journal of Modern Physics B*, vol. 19, no. 31, pp. 4525–4565, 2005.
73. J. Rosam, P. K. Jimack, and A. Mullis, "A fully implicit, fully adaptive time and space discretisation method for phase-field simulation of binary alloy solidification," *Journal of Computational Physics*, vol. 225, no. 2, pp. 1271–1287, 2007.
74. N. Provatas, N. Goldenfeld, and J. Dantzig, "Adaptive mesh refinement computation of solidification microstructures using dynamic data structures," *Journal of Computational Physics*, vol. 148, pp. 265–290, 1999.
75. N. Provatas, N. Goldenfeld, and J. Dantzig, "Efficient computation of dendritic microstructures using adaptive mesh refinement," *Physical Review Letters*, vol. 80, no. 15, p. 3308, 1998.
76. H. Gómez, V. M. Calo, Y. Bazilevs, and T. J. Hughes, "Isogeometric analysis of the cahn–hilliard phase-field model," *Computer methods in applied mechanics and engineering*, vol. 197, no. 49-50, pp. 4333–4352, 2008.
77. P. Deuflhard and F. Bornemann, *Scientific Computing with Ordinary Differential Equations*, vol. 42 of *Texts in Applied Mathematics*.
Berlin: Springer, 2002.
78. D. Kessler, R. H. Nochetto, and A. Schmidt, "A posteriori error control for the Allen–Cahn problem: Circumventing Gronwall's inequality," *Mathematical Modelling and Numerical Analysis (ESAIM: M2AN)*, vol. 38, no. 1, pp. 129–142, 2004.
79. G. Simsek, X. Wu, K. G. van der Zee, and E. H. van Brummelen, "Duality-based two-level error estimation for time-dependent PDEs: Application to linear and nonlinear parabolic equations," *Computer methods in applied mechanics and engineering*, vol. 288, pp. 83–109, 2015.